Manuscript prepared for Biogeosciences
with version 2014/07/29 7.12 Copernicus papers of the LaTeX class copernicus.cls.
Date: 11 March 2015

Shape of the Oceanic Nitracline

Melissa M. Omand[1,2] and Amala Mahadevan[1]

[1]Woods Hole Oceanographic Institution, Woods Hole, Massachusetts, USA.
[2]Currently at Graduate School of Oceanography, University of Rhode Island, Narragansett, Rhode Island, USA.

Correspondence to: Melissa M. Omand (momand@uri.edu)

Abstract. In most regions of the ocean, nitrate is depleted near surface by phytoplankton consumption and increases with depth, exhibiting a strong vertical gradient in the pycnocline (here referred to as the nitracline). The vertical supply of nutrients to the surface euphotic zone is influenced by the vertical gradient (slope) of the nitracline, and the vertical separation (depth) of the nitracline from the sunlit surface layer. Hence it is important to understand the shape (slope and curvature) and depth of the oceanic nitracline. By using density coordinates to analyze nitrate profiles from autonomous (APEX-ISUS floats) and ship-based platforms (WOA09, HOT, BATS and CalCOFI), we are able to eliminate much of the spatial and temporal variability in the profiles and derive robust relationships between nitrate and density. This allows us to characterize the depth, slope, and curvature of the nitracline in different regions of the world's oceans. The analysis reveals distinguishing patterns in the nitracline between subtropical gyres, upwelling regions and subpolar gyres. We propose a one-dimensional, mechanistic model that relates the shape of the nitracline to the relative depths of the surface mixed layer and euphotic layer. Though heuristic, the model accounts for some of the seasonal patterns and regional differences in the nitrate-density relationships seen in the data.

1 Introduction

Dissolved inorganic nitrate is an essential macro-nutrient for oceanic phytoplankton production. In the vast majority of the surface ocean that is sunlit, the production of phytoplankton is limited by the availability of nitrate. In such regions, consumption of nitrate by phytoplankton renders the sunlit ocean devoid of nitrate. Nitrate increases rapidly with depth in the underlying region, termed the *nitracline*, where it is resupplied through the remineralization of organic matter and redistributed along isopycnals by the ocean's circulation. The vertical supply of nitrate to the surface ocean depends not only on the vertical transport induced by dynamical processes like turbulent entrainment, Ekman pumping, and frontal and eddy-induced upwelling, but also on the vertical gradient of nitrate. Further, it depends on the depth from which nitrate needs to be drawn. Often, the isopycnal beneath which there is a significant vertical gradient of nitrate, termed the *nitrate-depletion density*, and its depth termed the *nitracline depth*, can be clearly distinguished. It is indicative of the density (and depth) from which nitrate must be transported into the euphotic layer, either by the (reversible) uplift of nitrate-rich isopycnals, or by (irreversible) advective and turbulent mechanisms.

One of the fundamental difficulties in finding generalized descriptions for the vertical distribution of nitrate is the high degree of variability in the nitrate-depth profiles. This may be partially overcome by exploiting the nitrate-density relationship that has long been known to be more robust than the relationship between nitrate and depth across the main pycnocline (*Redfield*, 1944; *Pytkowicz and Kester*, 1966). In some areas, the nutrient depleted near-surface layer transitions abruptly to a uniform gradient of nitrate with respect to density (termed *the nitracline slope*), whereas in others, the transition is more gradual, leading to curvature in the nitrate-density relationship. We term the slope and curvature of this relationship *the nitracline shape*. The shape and depth of the nitracline are pertinent to the vertical supply of nutrients for new phytoplankton production. The objective of this study is to characterize these properties of the nitracline from data and search for patterns and explanations for the revealed relationships.

Strickland (1970) was probably the first to find that over weeks, density could be used to predict nitrate to almost within experimental accuracy irrespective of the depth of the nutrient measurement. Recent studies (*Mcgillicuddy et al.*, 1999; *While and Haines*, 2010; *Ascani et al.*, 2013) have confirmed that nitrate is better correlated with density than with depth in the ocean. By relating isopycnal excursions with sea surface height *Ascani et al.* (2013) used the data from profiling floats to show that a higher variability of nitrate along isobars, as compared to isopycnals, on time scales ranging from hours to weeks, can be ascribed to the movement of isopycnal surfaces by internal waves and eddies. The relationship between nitrate and density also extends to longer space and time scales, leading to a large-scale alignment between the mean isopycnal and iso-nitrate surfaces (*Omand and Mahadevan*, 2013).

Since observations of nitrate are relatively rare and more difficult to obtain than measurements of temperature and salinity, a well characterized relationship between nitrate and density could be

useful in a number of applications ranging from modeling of primary production, where the initialization and restoration of nitrate is crucial to the interpretation of phytoplankton productivity from space. Several studies have exploited the nutrient-density relationship to develop descriptive algorithms for nitrate. *Elrod and Kester* (1985) applied a cubic spline method to produce reference curves for nutrient and oxygen in the Sargasso Sea. *Kamykowski and Zentara* (1986) developed third-order polynomial fits between nutrients and density (and nutrients and temperature) within 10° regions from the National Oceanographic Data Center (NODC) dataset. *Garside and Garside* (1995) used a step-wise polynomial method to predict nitrate from temperature and salinity during regional phenomena such as the North Atlantic spring bloom and El Niño/La Nina conditions in the central Pacific. Finally, first-order linear regressions between nitrate and temperature have been used to predict nitrate in upwelling zones (*Traganza et al.*, 1987; *Dugdale et al.*, 1997; *Olivieri and Chavez*, 2000; *Omand et al.*, 2012), although mixing and inter-leavening of water masses may confound this approach (*Friederich and Codispoti*, 1981). In coastal California, the relationship has been used to predict coastal nitrate concentration over the last century as an indicator of giant kelp health (*Parnell et al.*, 2010). Algorithms that exploit the nitrate-temperature relationship have also been developed for remotely-sensed sea surface temperature (SST) and ocean color (*Dugdale et al.*, 1989; *Goes et al.*, 2000; *Switzer et al.*, 2003), however the strong correlation between nitrate and temperature tends to break down near the surface as biological effects and upper ocean heat fluxes alter the relationship (*Garside and Garside*, 1995). Biological processes challenge the predictive capacity of the empirical algorithms and there are relatively few simple mechanistic models for oceanic nitrate distribution in density-coordinates (*Kamykowski*, 1987; *Dugdale et al.*, 1989; *Omand and Mahadevan*, 2013).

In this study, we draw from the growing dataset of nitrate measurements to glean a characterization and synthesis of the vertical distribution of nitrate. Vertical profiles of dissolved inorganic nitrate from shipboard sampling provide long time-series ($>$15 years) from programs such as the Hawaii Ocean Time-series (HOT), the Bermuda Atlantic Time-series Study (BATS), the California Cooperative Oceanic Fisheries Investigations (CalCOFI), and the compilation of climatological gridded datasets such as the World Ocean Atlas (WOA09 *Garcia et al.*, 2010). The more recently developed optical sensor, the *in situ* ultraviolet spectrophotometer (ISUS) (*Johnson and Coletti*, 2002), has facilitated high resolution *in situ* measurement of nitrate. By outfitting APEX autonomous profiling floats with such sensors, *Johnson et al.* (2013) are able to offer detailed sampling of the vertical distribution of nitrate in time (*Johnson et al.*, 2010). Such a growing database of nitrate measurements offers the opportunity to explore the vertical distribution of nitrate in space and time, and the regional variability in the shape and depth of the nitracline. Further, we can explore the relationship of the nitrate distribution to other parameters.

Here, we combine empirical and modeling approaches to describe the nitrate-density relationship. We apply second-order polynomial fits to the above datasets, diagnosing the nitrate depletion density,

the slope, and an index of curvature for the nitrate-density relationship. We develop an idealized model that predicts the curvature of the nitrate-density profile as a simple 1D function of the euphotic depth and mixed layer depth. We find that in the subtropical gyres, the shape may be predicted by the interplay between the depth of the mixed layer, the euphotic zone, and the remineralization depth. In some regions, however, upwelling, lateral mixing and transport by the large-scale circulation can complicate the relationship, rendering a one-dimensional approach less suitable. Finally, we discuss the the applications of this approach to ocean numerical modeling, and predictions of the vertical turbulent nitrate flux at the base of the euphotic zone.

2 Datasets

We used the publicly available nitrate ($\mathrm{NO_3}$) and potential density (σ_t) data from the World Ocean Atlas (WOA09), long-term time series (HOT, BATS, CalCOFI) and APEX-ISUS floats in the Pacific and Atlantic subtropical gyres. Only a brief description of each of these datasets is provided here.

2.1 World Ocean Atlas (WOA09)

We use the $5^\circ \times 5^\circ$ (n = 2448 gridded bins), annually averaged $\mathrm{NO_3}$ and σ_t, from the World Ocean Atlas (WOA09) (*Garcia et al.*, 2010) available through the National Oceanographic Data Center (http://www.nodc.noaa.gov/OC5/SELECT/dbsearch/dbsearch.html). The dataset compiles roughly 50 years of ship-based profiles of nitrate and density into a climatology by averaging data on a 5° grid and into 33 depth levels, with a vertical bin size that varies from 10 m near the surface to 400 m below 2000 m depth.

2.2 HOT, BATS and CalCOFI

The data set was constructed from the analysis of bottle samples of $\mathrm{NO_3}$ from monthly cruises between 1996 and 2012 at the deep-water Station ALOHA (A Long-Term Oligotrophic Habitat Assessment; 22°45'N, 158°00'W) located 100 km north of Oahu, Hawaii, at BATS (31°40' N 64°10' W) in the western Atlantic ocean, and from a 22 year record of quarterly measurements compiled from twelve CalCOFI (California Cooperative Oceanic Fisheries Investigations) stations (spanning 121.5 to 124.4° W and 30.5 to 32.7° N). The CalCOFI profiles are horizontally averaged over the region to generate a single time-series of profiles.

2.3 APEX-ISUS floats near Hawaii and Bermuda

Nitrate and potential density are obtained from two Webb Research APEX profiling floats (*Johnson et al.*, 2013); one deployed from December 4, 2009 (to present) at the ALOHA station near Hawaii (6401hawaii) and a second, deployed from November 6, 2009 to November 1, 2011 near the BATS station (6391bermuda). Each float collected a profile of conductivity, temperature, pressure, $\mathrm{NO_3}$ and

oxygen between the surface and the float's parking depth of 1000 m, with measurements vertically-spaced every ∼5 m (between 7 and 100 m depth) and 10 m (between 100 and 400 m), at roughly 5 day intervals (www.mbari.org/chemsensor/FloatList.html). Here, we examine only NO_3 and σ_t. Nitrate concentration is estimated with an in situ ultraviolet spectrophotometer (ISUS) with a short-term precision of about $\pm 0.1\ \mu M$, however over multi-year deployments, sensor drift introduces an additional uncertainty resulting in an accuracy of about $\pm 0.4\ \mu M$ (*Johnson et al.*, 2010, 2013).

3 Methods

The typical profile of NO_3 versus density in the ocean is described as follows: Within the least-dense, sunlit surface layer, nitrate is depleted due to uptake by phytoplankton. Across the main pycnocline, NO_3 increases with density, often reaching a subsurface maximum. In depth coordinates, this subsurface maximum in nitrate generally occurs between 500 and 1000 m, or intersects the seafloor. We focus on the nitrate-density relationship spanning the region of the main pycnocline that lies above the deep NO_3 maximum and beneath the NO_3 depletion density (Fig. 1a).

3.1 Second order polynomial fitting

Inspection of NO_3-σ_t profiles from various regions over the range described above reveals that while some profiles are very linear, others are not (Fig. 1b-g). We therefore seek a second order polynomial of the form $NO_3^\sigma = a\,(\sigma_t - \sigma_o)^2 + b\,(\sigma_t - \sigma_o) + c$ to describe the data from each region or location, and then compare the coefficients to distinguish regional characteristics. We subtract the density (σ_o) at the upper limit of the fit to minimize any effect in the fitting due to the mean value. Although using a higher-order polynomial would improve the fit skill, we restrict ourselves to a second-order polynomial because our goal is to characterize the most basic features of the NO_3-σ_t relationship in an effort to gain a mechanistic understanding of the processes that govern the nitracline shape and depth. In addition, for a number of the ocean time-series and WOA09 profiles, poor vertical resolution means that the inclusion of three or more parameters in the functional fit would increase the risk of over-fitting the data. The coefficients a, b, and c in the polynomial fit are obtained through a least squares minimization of

$$NO_{3k}^\sigma = a\,(\sigma_k - \sigma_o)^2 + b\,(\sigma_k - \sigma_o) + c, \quad k = 1, \ldots n \tag{1}$$

where k denotes each level in a profile, or areal average of profiles, n is the number of data points in the profile and NO_3^σ denotes the nitrate fit (in contrast to NO_3 which we use to denote data). The skill of each fit is evaluated over the bounded region, according to the normalized mean RMS error calculated as

$$\text{skill} = 1 - \sqrt{\frac{1}{n}\sum_{k=1}^{n} \frac{\left(NO_{3\,k} - NO_3^\sigma(\sigma_{t\,k})\right)^2}{NO_{3\,k}^2}}, \tag{2}$$

The slope of $NO_3^\sigma(\sigma_t)$ is given by $\frac{dNO_3^\sigma}{d\sigma_t} = 2a\,\sigma_t - b$. The 'linearity' of the profile can be estimated as the difference in the local slopes of NO_3^σ at either end of the profile $(2a\sigma_t - b)|_{k=1}^{k=n} = 2a(\sigma_{t\,k} - \sigma_{t\,1}) = 2a\Delta\sigma_t$, as compared with the slope over the entire profile $\frac{NO_3^\sigma(\sigma_{t\,n}) - NO_3^\sigma(\sigma_{t\,1})}{\sigma_{t\,n} - \sigma_{t\,1}} = \frac{\Delta NO_3}{\Delta\sigma_t}$. The ratio of these gives a dimensionless curvature index (the non-dimensionalized coefficient a) given by

$$a' = \frac{2a(\Delta\sigma_t)^2}{\Delta NO_3^\sigma}, \tag{3}$$

where ΔNO_3^σ and $\Delta\sigma_t$ denote the change in nitrate and density at either end of the profile. A large value of a' arises from a non-linear profile where the NO_3 gradient varies locally with σ_t. A small value of a' implies a linear profile with a constant gradient. Hence, we define three categories of fits. Those that are nonlinear ($a' > 1$), linear ($a' < 1$), and those that are poorly fit (skill< 0.8, due to higher order terms or scatter).

In the circumstance where the fits are linear ($a' < 1$), we also fit $NO_3^\sigma(\sigma_t)$ with a straight line of the form $NO_3^\sigma(\sigma_t) = b_{\rm lin}\,(\sigma_t - \sigma_o) + c_{\rm lin}$, where $b_{\rm lin}$ and $c_{\rm lin}$ are obtained from the least squares minimization of

$$NO_{3k} = b_{\rm lin}\sigma_k + c_{\rm lin}, \quad k = 1, \ldots n. \tag{4}$$

We can then find the nitrate depletion density $]\sigma_{depl}$ where NO_3^σ goes to zero as $\sigma_{t\,o} = -c_{\rm lin}/b_{\rm lin} + \sigma_o$. Similar to *Kamykowski and Zentara* (1986), we suggest that σ_{depl} represents the deepest isopycnal at which nitrate is depleted (or the nitrate depletion density). Since σ_t tends to be more highly resolved than discretely-sampled NO_3, this provides an appealing way of estimating of the nitracline depth z_o in circumstances where NO_3 is poorly vertically resolved or unavailable.

3.2 Fitting considerations

Particularly for nonlinear fits, the coefficients are sensitive to the upper and lower bounds of NO_3 that we select. For each profile, we aim to fit only the region beneath NO_3 depletion and above the NO_3 maximum with positive curvature. However, due to the large number of profiles, we tried to establish general criteria for the upper and lower extents of the fitted profile segments. As a shallow limit on the NO_3 fits, we retain only data with $NO_3 > 2\ \mu$M. This threshold generally distinguishes the NO_3-depleted surface samples in the discretely-sampled timeseries and WOA09 data, and falls sufficiently above the 0.4 μM accuracy of the ISUS sensors on the floats (*Johnson et al.*, 2013). The depth of this threshold varies spatially (Fig. 2a) and temporally, particularly in locations with strong seasonality in production, upwelling, (e.g., California current) or mixed layer depth (e.g., Bermuda). The deep bound on the NO_3-σ_t fits is qualitatively defined as some $\Delta\sigma_t$ above the deep NO_3 maximum. For the time series data (longterm stations and APEX-ISUS floats), we found that the NO_3 maxima tends to remain associated with a particular water density over time (for example see Figs. 6 and 7). We select thresholds of $\sigma_t < 26.75, 26.5, 27.2$ kg m^{-3} that fall roughly 0.5 kg m^{-3}

above the NO_3 maximum at CalCOFI, HOT, BATS, respectively. At HOT for example, this threshold was selected near the inflection point where NO_3 begins to curve downward (ie. see Fig. 6). The same thresholds as HOT and BATS are used for the corresponding APEX-ISUS float profiles. In the WOA09 climatology, the selection of a the deep threshold was more challenging, since each $5° \times 5°$ grid has different profile characteristics. Thus, we manually selected the lower bound on the fit for each grid by selecting the inflection point for each NO_3-σ_t profile individually. The inflection point is demonstrated in Fig. 1a, and the results for the lower bound on the WOA09 fits is shown in Fig. 2b.

The number of data points that are retained between the shallow and deep bounds described above, can also affect the fit coefficients, particularly a'. Through boot-strapping both the climatological and timeseries data we found that in general, the sensitivity of the results to a' were significantly diminished after the inclusion of 5 or more points in each fit. In the WOA09 climatology, the upper and lower bounds were selected to include at least 5 levels (Fig. 2c). The average number of data points used in the time series fits were 14 ± 5 (WOA09), 15 ± 8 (CalCOFI), 7 ± 5 (HOT), 8 ± 4 (BATS), 10 ± 2 (6391bermuda), 17 ± 3 (6401hawaii). For each fit, we evaluate the skill according to (2). Where the skill is poor (operationally defined here as < 0.8), the profiles are excluded from the analysis. In general, we find that the NO_3-σ_t skill exceeds 0.8 for nearly all of the WOA09 dataset (Fig. 2d) and 90% of the the time series profiles.

4 Results

In the following sections, we present results from the fitting method to describe global NO_3 and σ_t climatology (WOA09 $5° \times 5°$), and timeseries data from the California Current (CalCOFI), the North Atlantic Subtropical Gyre (BATS, APEX-ISUS float), and the North Pacific Subtropical Gyre (HOT, APEX-ISUS float). We analyze the fit coefficients (a, b, c), a', b_{lin} and c_{lin} to explore the spatial and temporal patterns and variability in these different records. We develop a simple 1D model for predicting a' from a balance between the mixed layer depth (z_{ML}) and euphotic depth (z_{eu}) and compare this with the subtropical APEX-ISUS data.

4.1 Nitrate-density fits from the WOA09 climatology

The nutrient depletion density σ_{depl} (Fig. 3a), shown along with fit coefficients a, b and c from the WOA09 climatology (Fig. 3b-d), is similar in pattern to the nitrate-depletion temperature described in *Kamykowski and Zentara* (1986) according to cubic regressions between NO_3 and temperature in $10°$ gridded climatology. Since this 1986 publication, roughly 700,000 new observations of NO_3 have been added to the National Oceanographic Data Center database. For comparison with the *Kamykowski and Zentara* (1986) results, we perform the same analysis between climatological WOA09 NO_3 and temperature (T) measurements. We find that the skill in NO_3-T (not shown)

has a very similar magnitude and distribution to the σ_t fits (Fig. 2d) and our method is not able to distinguish whether T or σ_t is a better proxy for NO_3.

We also compute a' for each $5^\circ \times 5^\circ$ grid (Fig. 4a). In 59% of these, we find that $a' < 1$ indicates a linear NO_3-σ_t relationship between the shallow and deep bounds of our fits. We observe a large-scale spatial coherence of a' in some regions. For example, we find that a' in the Eastern subtropical Pacific, throughout most of the Atlantic and the Northern Indian Ocean are predominantly less than one. In the Southern Ocean and the equatorial Pacific (incidentally regions that are less nitrate limited), a' tends to be larger than one, indicating curvature in NO_3-σ_t. The map of a' shows large variation between adjacent grid cells that are not attributable to known biogeographic boundaries. We explore the possibility that these results for a' were instead related to the number of points used in the fits (Fig. 2c) or lower skill (Fig. 2d) but these factors do not explain the variability. The WOA09 climatology is complied from profiles collected at different times of year and number of total samples. It is likely that some of the the variation between grids is a result of inhomogeneous sampling effort.

Where $a' < 1$, we find the slope (b_{lin}) according to (4) (Fig. 4b). In these locations (representing 59% of the climatology) the shape of the NO_3-σ_t relationship between nitrate depletion and the nitrate maximum is σ_t-independent and described by a single parameter b_{lin}. The slope varies from roughly 2 $\mu\mathrm{M\,m^3\,kg^{-1}}$, up to 18 $\mu\mathrm{M\,m^3\,kg^{-1}}$ at very high latitude. Some of the low values in the western tropical Pacific for example may be attributed to the large change in density (stratification) between the surface and depth of the nitrate maximum (≈ 150 m, Fig. 2b). Conversely, some higher values of b_{lin} correspond to regions where the upper bound on the NO_3 fits are deep (> 150 m, Fig. 2a).

4.2 Nitrate-density fits from the California current region (CalCOFI)

Several previous studies have identified a linear nitrate-temperature (NO_3-T) relationship beneath the nitrate-depletion density in the California current region (*Strickland*, 1970; *Parnell et al.*, 2010; *Omand et al.*, 2012). Profiles of NO_3-σ_t in the spatially-averaged quarterly CalCOFI record appear relatively consistent over time (green segments, Fig 5a). We compute a' for each profile and find that a' is consistently less than one, suggesting that the NO_3-σ_t relationship is linear over the 22 years analyzed (black points, Fig. 5b), and consistent with the WOA09 analysis which suggests that the relationship is relatively linear throughout the Eastern North Pacific Ocean below 50°N (Fig. 4a). Interannual variations are dominant over seasonal, and spatial variability in a' (Fig. 5b). The slope of the linear NO_3-σ_t fit (4) is shown for the annually, and spatially averaged record (Fig. 5c). The nutrient depletion density (σ_{depl}) varies interannually from 24.6 to 25.4 $\mathrm{kg\,m^{-3}}$ (black circles, Fig. 5d). The linear slope b_{lin} is correlated with σ_{depl} ($r^2 = 0.61$, $p < 0.001$), and is inversely correlated ($r^2 = .21$, $p < 0.001$) with the nutrient depletion temperature ($\mathrm{T_{depl}}$, red circles, Fig. 5d). We hypothesize that variations in b_{lin} and σ_{depl} may be related to the SST Nino index (yellow bars,

Fig. 5d), which assesses warming in the surface Ocean of the eastern Pacific. Indeed, some years do appear to have an above average $\mathrm{T_{depl}}$ (the 1998 El Niño) or low σ_{depl} (the 2004-2007) , however the pattern does not hold for all cases, indicating that there are additional drivers of the $\mathrm{NO_3}$-σ_t relationship.

4.3 Nitrate-density fits from HOT and float 6401hawaii

Monthly σ_t versus bottle-sampled $\mathrm{NO_3}$ from the HOT station at 22°45′N 158°00′W (Fig. 6a), is compared with a higher depth-and time-resolved σ_t versus $\mathrm{NO_3}$ record from a nearby APEX-ISUS float (6401hawaii), drifting over a nominally 400 km^2 region, centered at 23°N 161°W (Fig. 6b). The water column in this oligotrophic region remains stratified year-round, with near-surface (nominal 7 m) density fluctuations between 24 and 24.6 $\mathrm{kg\,m^{-3}}$, seen both in the HOT and APEX-ISUS records. Nutrient-depletion ($\mathrm{NO_3} < 2\ \mu\mathrm{M}$) occurs near the 25 $\mathrm{kg\,m^{-3}}$ isopycnal, and the nitrate maximum occurs near 27.1 $\mathrm{kg\,m^{-3}}$ (in 2012) over the 2.8 year record. Profiles of $\mathrm{NO_3}$-σ_t show a marked difference in shape from those in the California current. Over the fitted sections of each profile, $\mathrm{NO_3^\sigma}(\sigma_t)$ has positive curvature, with $a' > 1$ for 201 of the 206 total APEX-ISUS profiles and a' increasing from 1 to 2 (Fig. 6c).

Nitrate (color, Fig. 6d) within the shallow mixed layer (black line, Fig. 6d) is depleted year-round, and the base of the euphotic layer is consistently much deeper (around 180 m as indicated by the gray lines, Fig. 6d). Depth of the mixed layer, z_ML, and euphotic layer, z_eu, are obtained as described in the appendix.

4.4 Nitrate-density fits from BATS and float 6391bermuda

Monthly σ_t versus bottle-sampled $\mathrm{NO_3}$ from the BATS station at 31°40′N 64°10′W (Fig. 7a), and a more highly depth- and time-resolved σ_t versus $\mathrm{NO_3}$ record from a nearby APEX-ISUS float (6391bermuda), drifting over a nominally 600 km^2 region, centered at 32°N 66°W are shown in Fig. 7b. The surface (nominal 7 m depth) density of the Sargasso Sea fluctuates seasonally between 26.5 and 23.5 $\mathrm{kg\,m^{-3}}$ through deep winter convection and stratification in the summer. This 2 year record is punctuated by the passage of mesoscale eddies and wintertime storm events (*Lomas et al.*, 2013, and references therein). In contrast to the strong seasonality and transient events in the density structure, the overall relationship between $\mathrm{NO_3}$ and σ_t over our fitted region varies relatively little (colored regions, Fig. 7ab). The average linear slope (b_lin) is $32.3 \pm 4 \mathrm{kg\,m^{-3}}\,\mu\mathrm{M}^{-1}$. The deep nitrate maximum is centered at 27.3 $\mathrm{kg\,m^{-3}}$, and nitrate depletion occurs near the winter-time mixed layer potential density σ_t = 26.5 $\mathrm{kg\,m^{-3}}$. This depletion density corresponds to the density of the 18°C subtropical mode water. The production and advection of this water mass may alter downstream nutrient delivery (*Palter et al.*, 2005).

The $\mathrm{NO_3}$-σ_t relationship varies seasonally in both BATS and APEX-ISUS records. It is linear between January and July ($a' < 1$, green segments) and curved between August and December ($a' > 1$,

yellow segments). Scatter between successive a' tends to be small relative to the seasonal variation (Fig. 7c). Fluctuations in the nitracline depth due to deep mixing (*Steinberg et al.*, 2001) and mesoscale eddies (*McGillicuddy et al.*, 1998), though apparent in depth coordinates (Fig. 7d), are not distinguishable in density coordinates (Fig. 7ab). The mixed layer depth (z_{ML}, black line, Fig. 7d) is deepest in late winter (max. 380 m) and shoals to less than 10 m in the late summer. The euphotic depth (z_{eu}, gray lines, Fig. 7d) remains between 100 and 200 m, resulting in $|z_{\mathrm{eu}}| > |z_{\mathrm{ML}}|$ during the summer and $|z_{\mathrm{eu}}| < |z_{\mathrm{ML}}|$ for a portion of the winter. In the following section, we propose that in nitrate-limited systems, the nitracline shape may be controlled at first order by the depth of the euphotic layer relative to the mixed layer $z_{\mathrm{eu}} - z_{\mathrm{ML}}$.

5 A one-dimensional model of nitracline shape

Following (*Lewis et al.*, 1986), we model the vertical profile of nitrate assuming a balance between the vertical supply of nitrate to the euphotic layer, the uptake of nitrate by phytoplankton in the euphotic layer, and the resupply of nitrate by remineralization. This can be expressed as

$$\frac{\partial \mathrm{NO_3}(z)}{\partial t} = \frac{\partial}{\partial z}\left(\kappa(z)\frac{\partial \mathrm{NO_3}(z)}{\partial z}\right) - \alpha\, E_o\, e^{-kz}\, \gamma\, \mathrm{NO_3}(z) + R\, k_{rem}\, e^{-k_{rem} z}. \tag{5}$$

where $\kappa(z)$ represents the vertical eddy diffusivity, and $\kappa(z)\frac{\partial \mathrm{NO_3}}{\partial z}$ the vertical diffusive flux of nitrate, which is set to zero at the upper and lower boundaries. The uptake of nitrate is modeled as proportional to the initial slope of the photosynthesis-irradiance curve (α, $[\mu \mathrm{M m^2 W^{-1}}]$), the fraction of total nitrogen uptake that is supplied vertically in the form of nitrate (the "f-ratio", $\gamma\,\mathrm{NO_3}$), and the light profile, with the incident photosynthetically available irradiance (E_o $[\mathrm{W\,m^2}]$) attenuated exponentially according to a diffuse attenuation coefficient k ($[\mathrm{m^{-1}}]$, yellow shaded region, Fig. 8)). The euphotic depth is defined where the light attenuates to 1% of the incident level (E_o) such that $z_{\mathrm{eu}} = -log(0.01)k$. The $\mathrm{NO_3}$ uptake rate, μ, is comparable to phytoplankton growth rates ($\sim$ 0.1 to 2 $\mathrm{d^{-1}}$). Here, we use a low growth (uptake) rate $\mu = \alpha\gamma E_o = 0.17$ $\mathrm{d^{-1}}$ characteristic of subtropical gyres (*Maranon*, 2005). The remineralization of organic nitrogen to $\mathrm{NO_3}$ is modeled as the divergence of the vertical flux and taken to be exponential in depth (green shaded region, Fig. 8), with a vertical scale (k_{rem}^{-1}) of 250 m, which is typical of observed (*Lutz et al.*, 2002) and modeled (*Kwon et al.*, 2009) flux profiles. The magnitude of the flux R at z=0 is selected so that total $\mathrm{NO_3}$ is conserved, and the vertically integrated loss of $\mathrm{NO_3}$ due to uptake is balanced by the vertically integrated $\mathrm{NO_3}$ that is restored between the bottom of the domain, $z = -H$, and the surface, $z = 0$.

$$R = \frac{\alpha\, E_o\, \gamma \int_{-H}^{0} e^{-kz}\, \mathrm{NO_3}(z) dz}{k_{rem} \int_{-H}^{0} e^{-k_{rem} z}\, dz}. \tag{6}$$

We model the density as

$$\frac{\partial \sigma_t(z)}{\partial t} = \frac{\partial}{\partial z}\left(\kappa(z)\frac{\partial \sigma_t(z)}{\partial z}\right). \tag{7}$$

subject to a weak surface heat flux implemented as $\kappa(z)\frac{\partial \sigma_t(z)}{\partial z|_{z=0}} = C_p^{-1}\alpha_0\, q$, where C_p is the specific heat capacity of water [J-kg^{-1} °C^{-1}], α_0 is thermal expansion coefficient of water [°C^{-1}], and q is the surface heat flux [q=2 W m^{-2}].

The vertical eddy diffusivity $\kappa(z)$ is prescribed to be depth dependent and to enhance the vertical mixing over the mixed layer as

$$\kappa(z) = \kappa_{\min} + \kappa_{\max}\frac{1 - tanh(2\pi(z - z_{\rm ML})/z_{\rm w})}{2} \quad (8)$$

where $\kappa_{\min}$ and $\kappa_{\max}$ are the lower (deep) and upper (mixed layer) diffusivities, and $z_{\rm w}$ is a vertical length scale for the transition (here $z_{\rm w}$ = 200 m, though the results are not sensitive to this choice). We select $\kappa_{\max} = 10^{-4}$ m^{2}s^{-1} and $\kappa_{\min} = 10^{-5}$ m^{2}s^{-1}, values that are similar to *Lewis et al.* (1986). The modeled $\kappa(z)$ profile is shown in Fig. 8 (pink shaded region).

We solve (5) and (7) over a 1000 m (H) water column. We set σ_t to a constant value at $z = -H$, and prescribe a weak surface heat flux q, and but no surface or bottom flux of NO_3. In steady state, the divergence of the vertical NO_3 flux is balanced by uptake and remineralization. The two parameters that we vary are the mixed layer depth $z_{\rm ML}$ and the euphotic depth $z_{\rm eu}$. We find that the curvature of the NO_3-$\sigma_{\rm t}$ relationship depends strongly on these two free parameters.

We implement the model with $z_{\rm ML}$ and $z_{\rm eu}$ chosen to be typical of late winter at HOT (CASE 1: $z_{\rm ML}$=-30 m, $z_{\rm eu}$=-210 m) and BATS (CASE 2:$z_{\rm ML}$=-210 m, $z_{\rm eu}$=-80 m) stations. For CASE 1, $\sigma_{\rm t}$= 24.9 kg m^{-3} at the surface, with an upper and lower layer buoyancy frequency (N^2) of 1.3×10^{-5} and 5×10^{-5} s^{-2}, respectively (black line, Fig. 8a). In CASE 2, we maintain the same κ in the upper and lower layers, but the mixed layer is deeper, and $\sigma_{\rm t}$= 27.5 kg m^{-3} at the surface, reflecting the cooler surface water at BATS (black line, Fig. 8b). NO_3 it depleted near the surface in both cases due to uptake, with a subsurface maximum due to restoring (Fig. 8c,d). However, in CASE 2, uptake of NO_3 occurs only within the mixed layer, and so the large κ that operates on the density also acts to homogenize NO_3 over the same region, and both NO_3 and $\sigma_{\rm t}$ have a sharp transition near $z_{\rm ML}$. In contrast, CASE 1 has a deep euphotic layer, and so NO_3 uptake occurs below $z_{\rm ML}$ resulting in a smooth NO_3 transition approaching the surface. This difference is reflected in the different shapes of the NO_3-$\sigma_{\rm t}$ relationship (Fig. 8e,f), and is quantified using polynomial fits for estimating a' from (3) as was done for the data in the previous section. We fit the solution to a quadratic over the range $NO_3 > 0.5$ μM and $\sigma_t < 26.5$ and 27.2 kg m^{-3} following the lower bounds for HOT and BATS respectively. NO_3-$\sigma_{\rm t}$ for CASE 1 with $|z_{\rm ML}| < |z_{\rm eu}|$ is curved ($a' = 1.62$, Fig. 8e), whereas for CASE 2, $|z_{\rm ML}| > |z_{\rm eu}|$, the profile is linear ($a' = 0.05$, Fig. 8f). These curvatures of the profiles bear resemblance to randomly selected APEX-ISUS profiles from late winter 2010 (Fig. 8g,h) in the same regions. We also formulated the model with a light-saturating growth curve, but found that the steady-state solution remained unchanged.

We explore the dependance of the modeled a' on the parameter $z_{\rm ML} - z_{\rm eu}$. Keeping $z_{\rm ML} = 100$ m, $\kappa_{\max}$, $\kappa_{\min}$, $\kappa_{\rm w}$, k_{rem} and the boundary conditions fixed as for CASE 1, we obtain solutions to (5) and (7) over a range of $z_{\rm eu}$, from -10 to -300 m. We find a' from the polynomial fit between the

NO_3 and σ_t and solutions for each new z_{eu} (center black curve, Fig. 9). We find that the curvature index a' is a monotonically increasing function of $z_{ML} - z_{eu}$, with $a' \ll 1$ where z_{eu} is shallower than z_{ML}. Near $z_{ML} - z_{eu} = 70$ m, a' surpasses one, and increases steeply until leveling off near $a' = 2.5$. Our previous examples (CASE 1 and 2, Fig. 8) fall near this continuum on either side of the $a' = 1$ threshold. We test the sensitivity of these results to the μ and κ_{max} parameters by varying μ from 0.05 to 0.8 d^{-1} and κ_{max} from 2×10^{-5} to 4×10^{-4} $m^2 s^{-1}$. Increasing μ by a factor of four shifts the a' curve to the right, suggesting that the NO_3-σ_t relationship remains linear for a deeper z_{eu} than the previous cases (gray lines, Fig. 9). Conversely, decreasing μ by a factor of four shifts the curve to the left, indicating that a smaller difference between z_{ML} and z_{eu} is required before $a' > 1$. We find the a' is relatively insensitive to the choice of κ_{max} in the range 10^{-3} to 10^{-5} $m^2 s^{-1}$ (thin black lines, Fig. 9).

5.1 Model-data comparison

Our 1-D model predicts that when $|z_{eu}| < |z_{ML}|$, the nitracline shape is linear in density space ($a' \ll 1$) and when z_{eu} is significantly deeper than z_{ML}, the nitracline is curved ($a' > 1$). The model assumes that the divergence of the horizontal NO_3 flux is small compared with the vertical flux divergence, which may not be applicable in settings where lateral water mass intrusions strongly modify the profiles. It also assumes that at depth H=1000 m, σ_t remains fixed, and that NO_3 uptake balances remineralization over this depth range. Acknowledging the limitations of these assumptions, we plot the APEX-ISUS a' (black circles, Fig. 11) against the corresponding $z_{ML} - z_{eu}$ (appendix).

We find that for 6391bermuda, a' varies with z_{ML}-z_{eu} (Fig. 10b) but the relationship is scattered and also contains a hysteresis where the transition from $a' < 1$ to $a' > 1$ is delayed compared to the transition from deep to shallow mixed layers (see Fig. 7c,d). For 6401hawaii (Fig. 10b), the model fails to explain the variability in a' - reflected as an overall trend towards more positive a' (Fig. 6c). The scatter and independence of a' relative to our z_{ML}-z_{eu} index suggests that other processes or parameters are likely also important in determining the nitracline shape. However, the model does predict $a' > 1$ at Hawaii, and the much larger variability in a' at Bermuda, and the results generally fall within the model-predicted bounds (Fig. 10). Thus we conclude that a simple model similar to the one presented here may be a useful framework for understanding some of the basic features and differences in nitracline shape in different regions, particularly where nitrate is limiting, the horizontal gradients are relatively small, and variations in the deep nitrate supply are relatively steady.

6 Discussion

6.1 Nitrate in Ocean Models

The primary productivity in ecosystem models, and global carbon cycle models, relies strongly on the distribution of nitrate in the model. Datasets of nitrate are invaluable in initializing these models. If nitrate and density are initialized from concurrent measurements or a consistent data base, the nitrate-density relationship is implicit. In many instances, however, it would be advantageous to initialize the model's density field, and use a nitrate-density relationship for prescribing nitrate. This way, the $\mathrm{NO_3}$-σ_t relationship is maintained even if the model's density is altered. Treating nitrate in density coordinates is also useful if a restoring scheme is used for nutrients at depth.

6.2 Implications for estimating turbulent vertical fluxes of $\mathrm{NO_3}$

The turbulent vertical flux of $\mathrm{NO_3}$ ($F_{\mathrm{NO_3}}$) can be written as the product of the vertical eddy diffusivity, κ, and the vertical gradient in nitrate ($\partial\mathrm{NO_3}/\partial z$) according to

$$F_{\mathrm{NO_3}} = \kappa \frac{\partial \mathrm{NO_3}}{\partial z}. \tag{9}$$

The vertical eddy diffusivity, κ, is difficult to estimate. It may be inferred from tracers or microstructure measurements of the turbulent dissipation rate, ϵ (*e.g., Dewey and Crawford*, 1987). Based on observations of the relationship between shear production and buoyancy flux, κ is approximated by the relation (*Osborn*, 1980)

$$\kappa \leq \gamma \frac{\epsilon}{N^2}, \tag{10}$$

where γ is a mixing efficiency (approximately 0.2), the buoyancy frequency is $N^2 = -\frac{g}{\sigma_o}\frac{\partial \sigma_t}{\partial z}$, and ϵ is the turbulent kinetic energy dissipation rate. Applying the chain rule to (8) whereby $\frac{\partial \mathrm{NO_3^*}}{\partial z} = \frac{\partial \mathrm{NO_3^*}}{\partial \sigma_t}\frac{\partial \sigma_t}{\partial z}$, and substituting (9) into (8), the N^2-dependence cancels, yielding

$$F_{\mathrm{NO_3}} \sim \epsilon \frac{\partial \mathrm{NO_3^*}}{\partial \sigma_t}. \tag{11}$$

We expect that $F_{\mathrm{NO_3}}$ will be proportional to ϵ and the gradient of $\mathrm{NO_3}$ across isopycnals. The turbulent flux of $\mathrm{NO_3}$ near the base of the euphotic zone is of particular interest as the $\mathrm{NO_3}$ flux into the euphotic zone supports new primary production in many oceanic regions. The striking temporal consistency in the $\mathrm{NO_3}$-σ_t relationship from this analysis, suggests that this relation could prove useful for estimating vertical $\mathrm{NO_3}$ fluxes from ϵ, which unlike κ, can be directly measured.

6.3 Depth of the nitracline

One way of defining the depth of the nitracline is to use a nitrate cutoff and test for the depth where the nitrate crosses this value. This may lead to noisy results, because nitrate can be highly variable

within the euphotic layer, and the vertical resolution of the data may be insufficient to identify the cutoff depth. *Aksnes et al.* (2007) used a novel approach of relating nitrate in the near-surface ocean to the attenuation profile of light by solving a one-dimensional equation in which the uptake of nitrate by phytoplankton is linearly related to light and nitrate itself. Since light decays exponentially with a characteristic attenuation coefficient, the depth and slope of the nitracline can be related to the attenuation characteristics of light, which are easily measured. Here, we suggest that by fitting the nitrate to density, one can identify the nutrient depletion density σ_{to} where $\mathrm{NO}_3^* = 0$, and thereby identify the depth of the isopycnal σ_{to} as the depth of the nitracline. This gives robust results when the NO_3-σ_t relationship is linear, in which case, $\sigma_{to} = b_\mathrm{lin}/c_\mathrm{lin}$.

7 Conclusions

Having examined nitrate profiles from several sources, the WOA09 gridded data, BATS, HOTS, CalCOFI time series, and float records from Bermuda and Hawaii, we find that the NO_3-σ_t relationship can be characterized using a second order polynomial to fit the data. The non-dimensional curvature a', serves as a measure of non-linearity of the relationship. When linear, $a' < 1$ and the slope of the profile can be identified, as can the nitrate depletion density and nitracline depth. A simple one-dimensional model is able to explain the nitracline shape ($a' < 1$ or $a' > 1$) in terms of the depth of the euphotic layer z_eu and mixed layer depth z_ML. When $|z_\mathrm{eu}| - |z_\mathrm{ML}| > 100$m, $a' > 1$. Conversely, when $|z_\mathrm{eu}| - |z_\mathrm{ML}| < 100$m, $a' < 1$. Though the model makes the assumption of one-dimensionality, we find that $|z_\mathrm{eu}| - |z_\mathrm{ML}|$ is broadly indicative of whether the NO_3-σ_t relationship is linear or curved in the subtropical gyre data. The model relies on the assumption of weak variation in lateral nitrate supply, and thus may not be applicable in more complex regions. It is advantageous to examine NO_3 in an isopycnal coordinate system as compared to depth coordinates, because variability due to vertical mixing and advection affect NO_3 and σ_t in a similar way, while generally maintaining the characteristics of the NO_3-σ_t relationship. With the growing database of nitrate ffrom ship-based and autonomous platforms, a more detailed picture will undoubtably emerge and provide the opportunity to refine our understanding of the underlying processes that govern nitracline shape and nitrate supply to the surface ocean.

8 Appendix

The mixed layer depth (z_ML) is computed from monthly CTD profiles as the depth where the density difference is 0.03 $\mathrm{kg\,m^{-3}}$ from the near-surface density and then is smoothed with a 90 day low-pass filter. At HOT, the pycnocline is present year-round and z_ML varies between -20 and -80 m on sub-seasonal timescales (Fig. 6d). At BATS, stratification is eroded during the winter as the surface loses heat, and wind and wave-driven turbulence mix the upper water column to depths ranging between

-200 and -400 m. During the summer, an intense pycnocline develops and z_{ML} shoals to less than -20 m (Fig. 7d).

The euphotic depth (z_{eu}) is defined as the level where photosynthetically available radiation (PAR) is 1% of the surface PAR. Because *in situ* PAR is not measured at HOT, BATS or on the APEX-ISUS floats, z_{eu} is estimated two ways; 1) from the depth-integral of $\mathrm{Chl}a$ following *Morel* (1988) and *Morel and Berthon* (1989), henceforward referred to MB (solid gray line, Fig. 6d and 7d), and 2) from the Moderate Resolution Imaging Spectroradiometer (MODIS) level 3 K490 satellite product (dashed gray line, Fig. 6d and 7d).

At the time series stations BATS and HOT, the CTD-based profiles of $\mathrm{Chl}a$ fluorescence are calibrated to *in situ* samples of pigment concentration. MB established a statistical relationship between surface-normalized photosynthetically available radiation (PAR), and the depth-integrated $\mathrm{Chl}a$ content ($\langle \mathrm{Chl}a \rangle$) in the water column for Case 1 waters. The relationship between $z_{\mathrm{eu\,MB}}$ and $\langle \mathrm{Chl}a \rangle$ was approximated with the curves.

$$z_{\mathrm{eu\,MB}} = \begin{cases} -568.2 \langle \mathrm{Chl}a \rangle^{-0.746} & \text{for } z_{\mathrm{eu\,MB}} > -102\,\mathrm{m} \\ \\ -200.0 \langle \mathrm{Chl}a \rangle^{-0.293} & \text{for } z_{\mathrm{eu\,MB}} < -102\,\mathrm{m} \end{cases}$$

The appropriate depth over which to integrate $\mathrm{Chl}a$ in the above expression, is determined iteratively, first using $\langle \mathrm{Chl}a \rangle$ integrated between the surface and 400 m. The $z_{\mathrm{eu\,MB}}$ is used as the next limit of integration for $\langle \mathrm{Chl}a \rangle$. This process is repeated until the solution for $z_{\mathrm{eu\,MB}}$ converges.

Satellite-derived euphotic depth ($z_{\mathrm{eu\,sat}}$) was determined from $z_{\mathrm{eu\,sat}} = -4.6/\mathrm{K490}$, where the 8-day, level 3, MODIS K490 is spatially averaged over a $10^{\circ} \times 10^{\circ}$ region centered on the BATS and HOT stations. At BATS, both $z_{\mathrm{eu\,MB}}$ and $z_{\mathrm{eu\,sat}}$ vary seasonally, becoming shallower during the winter and deepening during the summer. The $z_{\mathrm{eu\,MB}}$ is based on *in situ* measurements of $\mathrm{Chl}a$ throughout the water-column, whereas K490 is a function of the water-leaving radiance over the first optical depth ($a' prox z_{\mathrm{eu}}/4.6$). Both are approximations of the true z_{eu}, and differences between $z_{\mathrm{eu\,sat}}$ and $z_{\mathrm{eu\,MB}}$ reflect the methodological differences. The $z_{\mathrm{eu\,sat}}$ integrates water-leaving irradiance over a shallow portion of the water column - roughly 5 to 20 m thick, whereas $z_{\mathrm{eu\,MB}}$ integrates over the entire water column.

For example in spring 2010 at BATS, a subsurface maximum in $\mathrm{Chl}a$ developed that led to shoaling of $z_{\mathrm{eu\,MB}}$ (solid gray line, Fig. 7d), these events were not evident in $z_{\mathrm{eu\,sat}}$, possibly because this subsurface layer was not visible within the satellite penetration depth. For the model-data comparison in Section 5.1 (Fig. 11), we use $z_{\mathrm{eu\,sat}}$. The variation in z_{ML}-z_{eu} at Bermuda are driven primarily by variation in z_{ML}, and so our analysis was not sensitive to this choice.

Acknowledgements. We acknowledge the support of the National Science Foundation (Grant OCE-0928617) and NASA (Grant NNX-08AL80G). This manuscript benefited from discussions with David Nicholson, Su-

san Lozier and Emily Shroyer. We thank Anand Gnanadesikan for insightful feedback that led to substantial improvements.

References

Aksnes, D. L., M. D. Ohman, and P. Riviere, Optical effect on the nitracline in a coastal upwelling area, *Limnology and Oceanography*, *52*(3), 1179–1187, 2007.

Ascani, F., K. J. Richards, E. Firing, S. Grant, K. S. Johnson, Y. Jia, R. Lukas, and D. M. Karl, Physical and biological controls of nitrate concentrations in the upper subtropical North Pacific Ocean, *Deep Sea Research Part II: Topical Studies in Oceanography*, 2013.

Dewey, R. K., and W. R. Crawford, A microstructure instrument for profiling oceanic turbulence in coastal bottom boundary layers, *J. Atmos. Ocean. Technol.*, *4*(2), 288–297, 1987.

Dugdale, R. C., M. Andre, A. Bricaud, and F. P. Wilkerson, Modeling New Production in Upwelling Centers: A Case Study of Modeling New Production From Remotely Sensed Temperature and Color, *Journal of Geophysical Research*, *94*, 18,119–18,132, 1989.

Dugdale, R. C., C. O. Davis, and F. P. Wilkerson, Assessment of new production at the upwelling center at Point Conception, California, using nitrate estimated from remotely sensed sea surface temperature, *Journal of Geophysical Research*, *102*(C4), 8573–8585, 1997.

Elrod, J. A., and D. R. Kester, Sargasso Sea reference curves for salinity, potential temperature, oxygen, nitrate, phosphate, and silicate as functions of sigma-theta, *Deep-Sea Research*, *32*, 391–405, 1985.

Friederich, G. E., and L. A. Codispoti, *The effects of mixing and regeneration on the nutrient content of upwelling waters off Peru*, 221-227 pp., American Geophysical Union, 1981.

Garcia, H. E., R. A. Locarnini, T. P. Boyer, J. I. Antonov, M. M. Zweng, O. K. Baranova, and D. R. Johnson, *World Ocean Atlas 2009, Volume 4: Nutrients (phosphate, nitrate, silicate)*, S. Levitus, Ed. NOAA Atlas NESDIS 71, U.S. Government Printing Office, 2010.

Garside, C., and J. C. Garside, Euphotic-zone nutrient algorithms for the NABE and EqPac study sites, *Deep-Sea Research II*, *42*(2-3), 335–347, 1995.

Goes, J. I., T. Saino, H. Oaku, J. Ishizaka, C. S. Wong, and Y. Nojiri, Basin scale estimates of sea surface nitrate and new production from remotely sensed sea surface temperature and chlorophyll, *Geophysical Research Letters*, *27*(9), 1263–1266, 2000.

Johnson, K. S., and L. J. Coletti, In situ ultraviolet spectrophotometry for high resolution and long-term monitoring of nitrate, bromide and bisulfide in the ocean, *Deep-Sea Research Part I*, *49*, 1291–1305, 2002.

Johnson, K. S., S. C. Riser, and D. M. Karl, Nitrate supply from deep to near-surface waters of the North Pacific subtropical gyre, *Nature*, *465*(7301), 1062–1065, 2010.

Johnson, K. S., L. J. Coletti, H. W. Jannasch, C. M. Sakamoto, D. D. Swift, and S. C. Riser, Long-term nitrate measurements in the ocean using the In Situ Ultraviolet Spectrophotometer: sensor integration into the APEX profiling float, *Journal of Atmospheric and Oceanic Technology*, *30*, 1854–1866, 2013.

Kamykowski, D., A preliminary biophysical model of the relationship between temperature and plant nutrients in the upper ocean, *Deep-Sea Research*, *34*(7), 1067–1079, 1987.

Kamykowski, D., and S.-J. Zentara, Predicting plant nutrient concentrations from temperature and sigma-t in the upper kilometer of the world ocean, *Deep-Sea Research*, *33*(1), 99–105, 1986.

Lewis, M. R., W. G. Harrison, N. S. Oakey, D. Herbert, and T. Platt, Vertical Nitrate Fluxes in the Oligotrophic Ocean, *Science*, *234*, 870–873, 1986.

Lomas, M., N. Bates, R. Johnson, A. Knap, D. Steinberg, and C. Carlson, Two decades and counting: 24-years of sustained open ocean biogeochemical measurements in the Sargasso Sea, *Deep Sea Research Part II: Topical Studies in Oceanography*, *93*, 16 – 32, 2013.

Lutz, M., R. Dunbar, K. Caldeira, Regional variability in the vertical flux of particulate organic carbon in the ocean interior *Global Biogeochemical Cycles*, *16*, 3, 2002.

Maranon, E., Phytoplankton growth rates in the Atlantic subtropical gyres, *Limnology and Oceanography*, *50*, 299–310, 2005.

McGillicuddy, D. J., A. R. Robinson, D. A. Siegel, H. W. Jannasch, R. Johnson, T. D. Dickey, J. McNeil, A. F. Michaels, and A. H. Knap, Influence of mesoscale eddies on new production in the Sargasso Sea, *Nature*, *394*, 263–266, 1998.

Mcgillicuddy, D. J., Jr, R. Johnson, D. A. Siegel, A. F. Micheals, N. R. Bates, and A. H. Knap, Mesoscale variations of biogeochemical properties in the Sargasso Sea, *Journal of Geophysical Research*, *104*(C6), 13–389–13–394, 1999.

Morel, A., Optical modeling of the upper ocean in relation to its biogenous matter content (case I waters), *Journal of Geophysical Research*, *93*, 10,749–10,768, 1988.

Morel, A., and J.-F. Berthon, Surface pigments, algal biomass profiles, and potential production of the euphotic layer: Relationships reinvestigated in view of remote-sensing applications., *Limnology and Oceanography*, *34*, 1545–1562, 1989.

Olivieri, R., and F. Chavez, A model of plankton dynamics for the coastal upwelling system of Monterey Bay, California, *Deep-sea research. Part 1. Oceanographic research papers*, *47*(5), 1077–1106, 2000.

Omand, M., and A. Mahadevan, Large-scale alignment of oceanic nitrate and density, *Journal of Geophysical Research, in press*, 2013.

Omand, M. M., F. Feddersen, R. T. Guza, and P. J. S. Franks, Episodic vertical nutrient fluxes and nearshore phytoplankton blooms in Southern California, *Limnology and Oceanography*, *57*(6), 2012.

Osborn, T. R., Estimates of the local rate of vertical diffusion from dissipation measurements, *J. Phys. Oceanogr.*, *10*, 83–89, 1980.

Palter, J. B., M. S. Lozier, and R. T. Barber, The effect of advection on the nutrient reservoir in the North Atlantic subtropical gyre, *Nature*, *437*(7059), 687–692, 2005.

Parnell, P. E., E. F. Miller, C. E. Lennert-Cody, P. K. Dayton, and M. L. Carter, The response of giant kelp (Macrocystis pyrifera) in southern California to low-frequency climate forcing, *Limnology and Oceanography*, *55*(6), 2686–2702, 2010.

Pytkowicz, R. M., and D. R. Kester, Oxygen and phosphate as indicators for the deep intermediate waters in the northeast Pacific Ocean, *Deep-Sea Research*, *13*, 373–379, 1966.

Redfield, A. C., The processes dertermining the concentration of oxygen, phosphate and other organic derivatives within the depths of the Atlantic Ocean, *Papers in Physical Oceanography and Meteorology*, *9*, 1–22, 1944.

Kwon, E. W., Primeau, F., and Sarmiento, J. L., The impact of remineralization depth on the air-sea carbon balance,*Nature Geoscience*, *2*, 630–635, 2009.

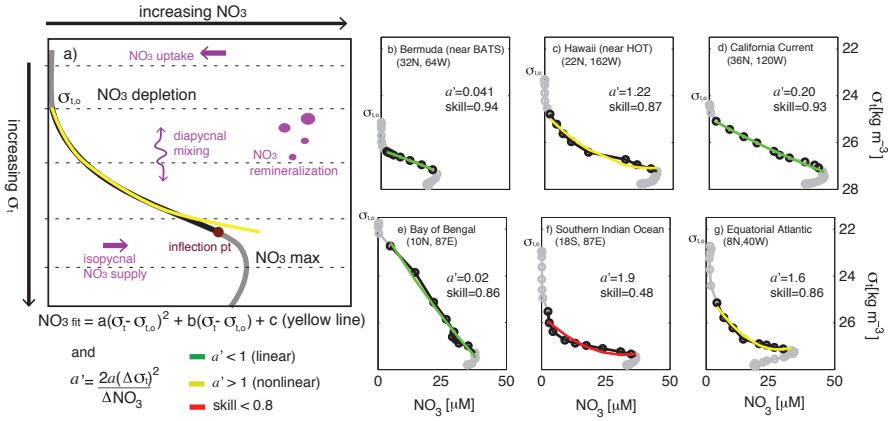

Figure 1. a) Schematic of a typical oceanic NO_3 versus σ_t profile. In nitrate-limited regions, near-surface (low density) NO_3 is near zero above a nitrate depletion density and tends to increase monotonically with increasing σ_t until reaching a subsurface NO_3 maximum. The region below NO_3 depletion and above the inflection point (where NO_3 begins to curve downward towards the maximum, black segment) is evaluated with a second order polynomial (NO_3^{σ}, yellow line), where a' is an index of curvature. b) to g) show examples from the WOA09 climatology (circles) with black circles indicating those that are used in the fits. Colored lines indicate $a' < 1$ (green), $a' > 1$ (yellow) or skill<0.8 (red).

Steinberg, D. K., C. A. Carlson, N. R. Bates, R. J. Johnson, A. F. Michaels, and A. H. Knap, Overview of the US JGOFS Bermuda Atlantic Time-series Study (BATS): A decade-scale look at ocean biology and biogeochemistry, *Deep Sea Research Part II: Topical Studies in Oceanography*, *48*, 1405 – 1447, 2001.

Strickland, J. D., *The Ecology of the Plankton Off La Jolla, California, in the Period April Through September, 1967*, vol. 17, Bulletin of the Scripps Institution of Oceanography, 1970.

Switzer, A. C., D. Kamykowski, and S.-J. Zentara, Mapping nitrate in the global ocean using remotely sensed sea surface temperature, *Journal of Geophysical Research*, *108*(C8), 3280, 2003.

Traganza, E. D., D. G. Redalije, and R. W. Garwood, Chemical flux, mixed layer entrainment and phytoplankton blooms at upwelling fronts in the California coastal zone, *Continental Shelf Research*, *7*(1), 89–105, 1987.

While, J., and K. Haines, A comparison of the variability of biological nutrients against depth and potential density, *Biogeosciences*, *7*, 1263–1269, 2010.

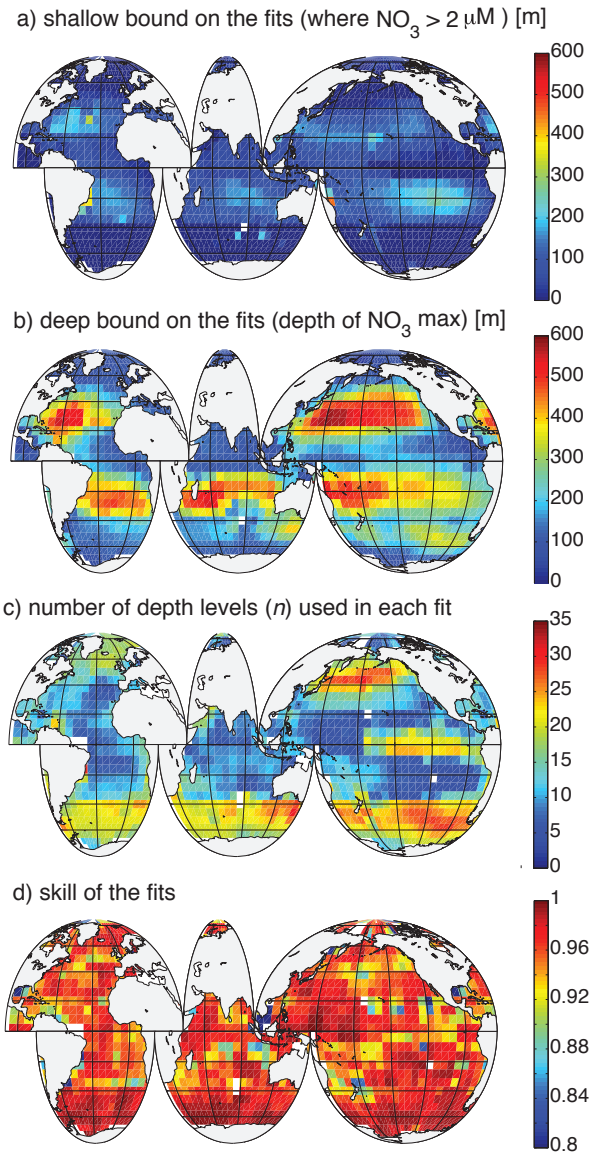

Figure 2. Global maps from the 5° WOA09 climatology indicating the (a) depth of the upper limit ($\mathrm{NO_3} > 2\ \mu\mathrm{M}$), (b) subsurface $\mathrm{NO_3}$ maximum, (c) number of depth levels that fell between the depths in (a) and (b) and were used in each fit, (d) skill of the polynomial fit to the data evaluated as skill $= 1 - \sqrt{\frac{1}{n}\sum_{k=1}^{n}\frac{\left(\mathrm{NO_3}_k - \mathrm{NO_3^\sigma}(\sigma_t{}_k)\right)^2}{\mathrm{NO_3^2}_k}}$.

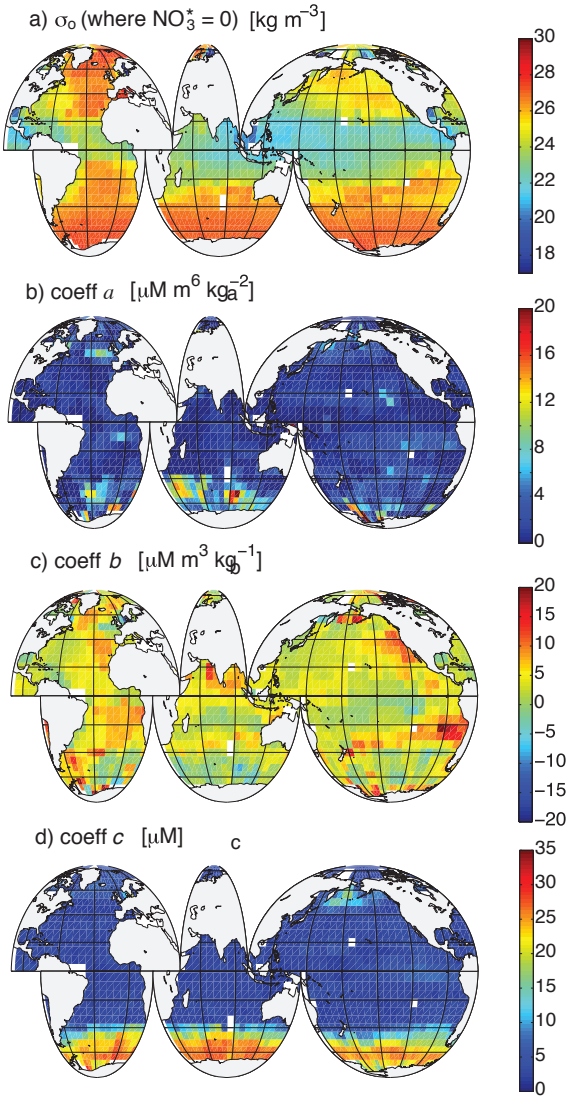

Figure 3. Global maps from the 5° WOA09 climatology showing the (a) the nitrate depletion density (σ_o, where $\mathrm{NO}_3^\sigma = 0$), and the polynomial fit coefficients (a) a, (b) b, (c) c from (1).

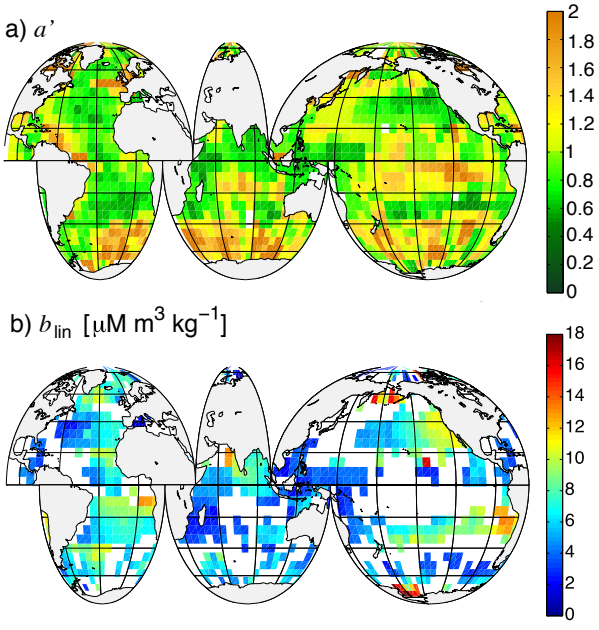

Figure 4. Global maps from the 5° WOA09 climatology of (a) a' and (b) b_{lin} where $a' < 1$. Green regions ($a' < 1$) in panel a indicate a linear NO_3-σ_t fit.

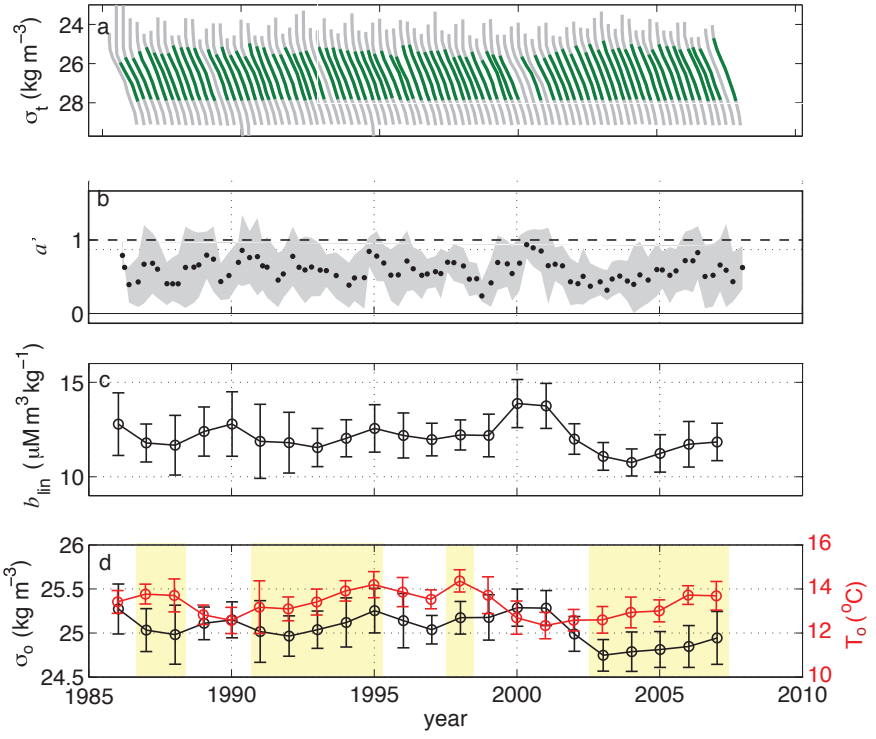

Figure 5. (a) Successive profiles of NO_3 as a function of σ_t from quarterly CalCOFI cruises. Green segments indicate the portion of each profile that is fit with (1), and profiles without green segments have a fit skill < 0.8. (b) a' (black dots) for each of the profiles from a). Annual averages of the (c) slope $b_{\rm lin}$ and (d) intercepts σ_{to} (black) and T_o (red) of linear σ_t-NO_3 fits (4), with errors bars indicating the standard deviation from the spatial and temporal averaging. Yellow shaded regions in (d) indicate the time periods with a positive SST anomaly in the Nino-3.4 region associated with El Niño conditions.

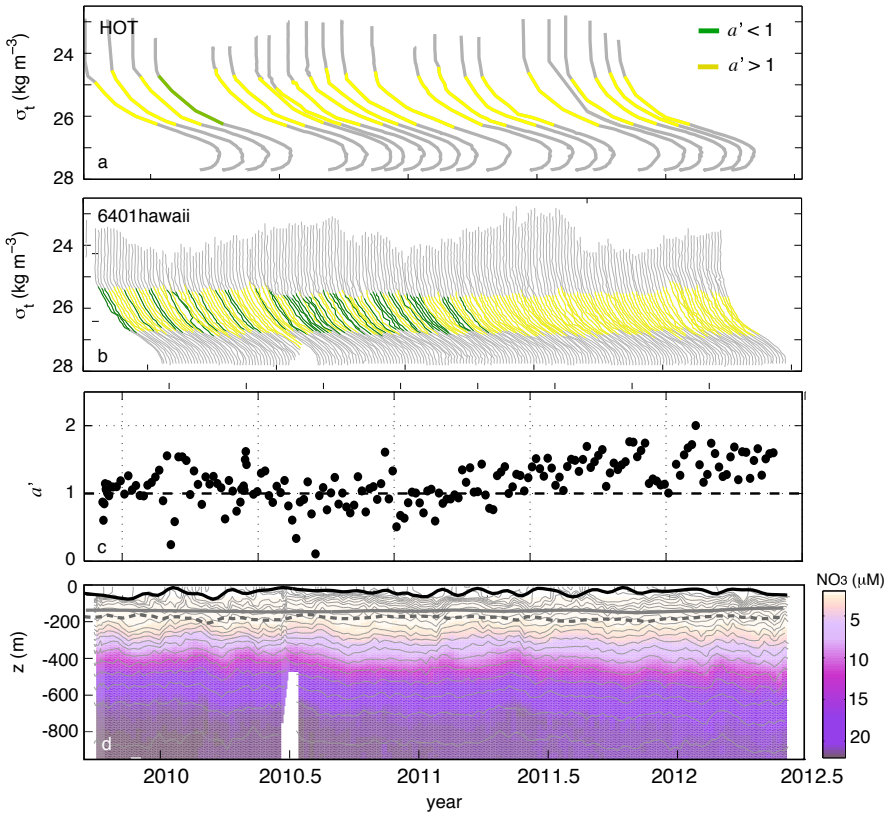

Figure 6. Successive profiles of NO_3 as a function of σ_t, from (a) the monthly HOT timeseries and (b) an APEX-ISUS float (6401hawaii) deployed nearby from December 2009 to June 2012, profiling at 5 day intervals. Green and yellow segments indicate $a' < 1$ and $a' > 1$ respectively (skill > 0.8). (c) a' for each of the APEX-ISUS profiles in (b). (d) Depth-resolved timeseries of NO_3 (colors) with σ_t contours overlaid. The mixed layer depth z_{ML} and the euphotic depth z_{eu} are shown with the black and gray lines respectively. The solid and dashed gray lines represent different approximations of z_{eu} (see appendix).

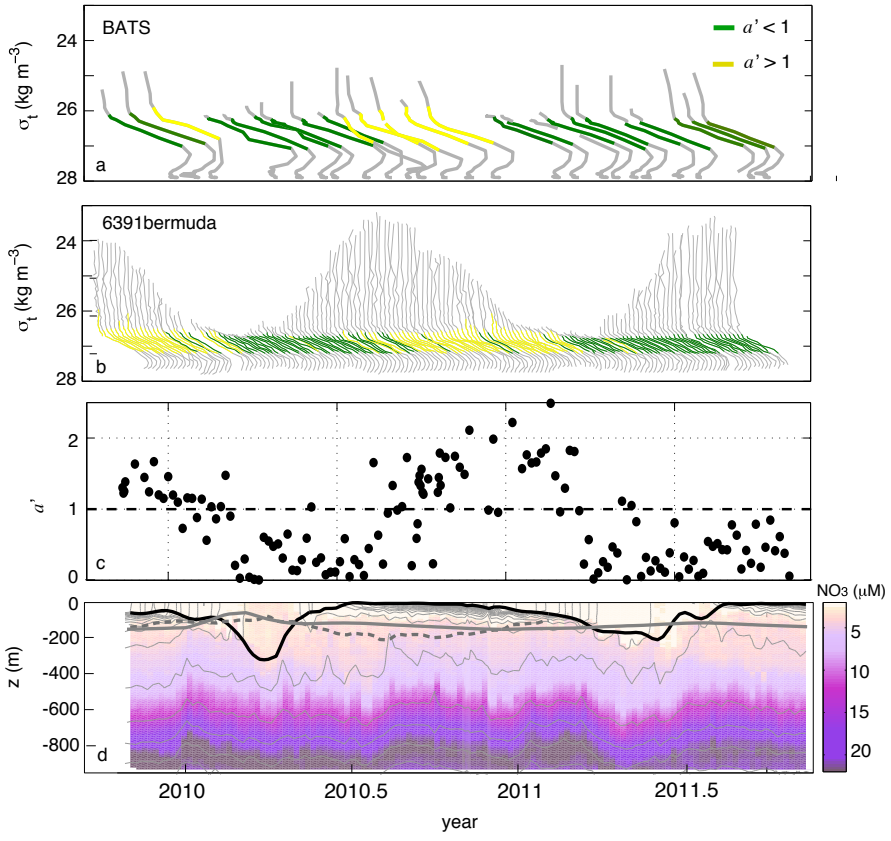

Figure 7. Successive profiles of NO_3 as a function of σ_t, from (a) the monthly BATs timeseries and (b) an APEX-ISUS float (6391bermuda) deployed nearby from November 2009 to November 2011 profiling at 5 day intervals. Green and yellow segments indicate $a' < 1$ and $a' > 1$ respectively (skill > 0.8). (c) a' for each of the APEX-ISUS profiles in (b). (d) Depth-resolved timeseries of NO_3 (colors) with σ_t contours overlaid. The mixed layer depth z_{ML} and the euphotic depth z_{eu} are shown with the black and gray lines respectively. The solid and dashed gray lines represent different approximations of z_{eu} (see appendix).

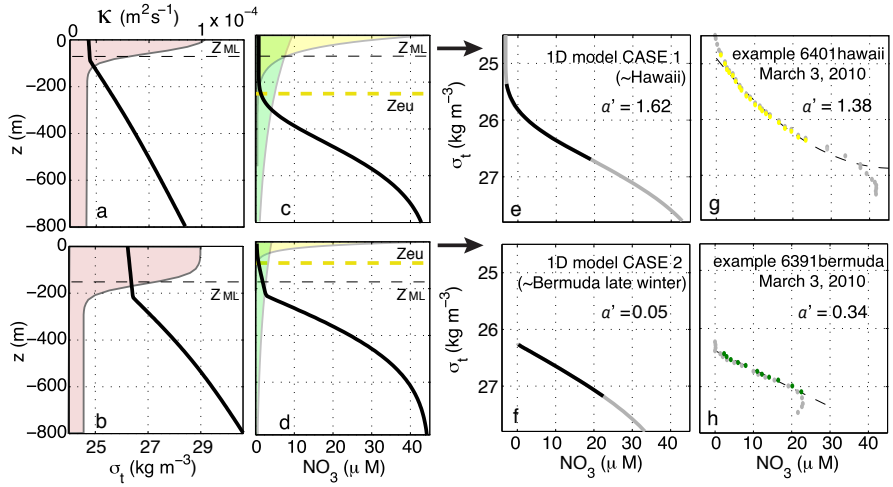

Figure 8. Examples of profiles of σ_t (a and b) and NO_3 (c and d) produced with the simple 1D model. The mixed layer depth (z_{ML}) and the euphotic depth (z_{eu}) are chosen to represent typical conditions near Hawaii (with a shallow $z_{ML} = -30$ m and deep $z_{eu} = -210$ m, upper panels "CASE 1") and near Bermuda during late winter (with a deep $z_{ML} = 180$ m and shallow $z_{eu} = 80$ m, lower panels "CASE 2"). The shaded regions in panels a-d indicate the shape of the depth-variable diapycnal eddy diffusivity κ (pink), the shape of the irradiance profile (yellow), and the remineralization curve (green) used in the model. The modeled σ_t-NO_3 relationship is shown for e) CASE 1 and f) CASE 2, and can be compared to fitted profiles from the APEX-ISUS floats from late winter, 2010 (panels g,h).

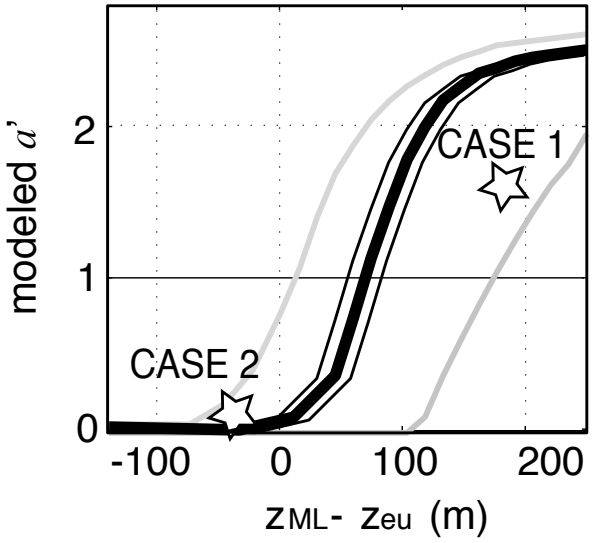

Figure 9. The model-derived a' over a range of $z_{ML} - z_{eu}$ with a growth rate (μ_o) of 0.2 d^{-1} (black curve). The location of the curve depends on the μ_o selected, μ = 2 d^{-1} shifts the curve right (gray line to the right) and μ = 0.02 d^{-1} shifts it left (gray line to the left). The thin black lines show the model sensitivity to varying upper layer κ. The stars indicate the value of $z_{ML} - z_{eu}$ and a' from CASES 1 and 2.

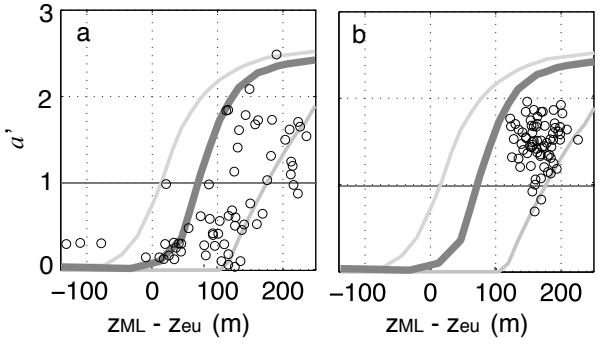

Figure 10. The a' from the APEX-ISUS NO_3-σ_t fits at (a) Hawaii and (b) Bermuda, versus $z_{ML} - z_{eu}$ for each profile (black circles). The method for obtaining approximate z_{ML} and z_{eu} at each profile is described in the appendix. These observed a' are overlaid on the model prediction from Fig. 9.